Available online at www.sciencedirect.com
ScienceDirect
Advances in Water Resources 30 (2007) 2339–2353
Advances in Water Resources
www.elsevier.com/locate/advwatres

Capillary pressure for the sand–CO_2–water system under various pressure conditions. Application to CO_2 sequestration

W.-J. Plug *, J. Bruining

Delft University of Technology, Civil Engineering and Geosciences, Mijnbouwstraat 120, 2628 RX Delft, Netherlands

Received 9 October 2006; received in revised form 21 May 2007; accepted 22 May 2007
Available online 8 June 2007

Abstract

Accurate modeling of storage of carbon dioxide (CO_2) in heterogeneous aquifers requires experiments of the capillary pressure as function of temperature and pressure. We present a method with which static drainage and imbibition capillary pressures can be measured continuously as a function of saturation at various temperature (T) and pressure (P) conditions. The measurements are carried out at (T, P) conditions of practical interest. Static conditions can be assumed as small injection rates are applied. The capillary pressure curves are obtained for the unconsolidated sand–distilled water–CO_2 system. The experimental results show a decrease of drainage and imbibition capillary pressure for increasing CO_2 pressures and pronounced dissolution rate effects for gaseous CO_2. Significant capillary pressure fluctuations and negative values during imbibition are observed at near critical conditions. The measurement procedure is validated by a numerical model that simulates the experiments.

Keywords: Capillary pressure; Carbon dioxide; Quasi-static; High pressures; Mass transfer; CO_2 sequestration

1. Introduction

There is increasing evidence that the emission of CO_2 contributes to the global warming problem. Geological storage of CO_2 in deep (saline) aquifers, abandoned hydro-carbon reservoirs and unminable coal seams (Enhanced Coal Bed Methane) has the potential to reduce the problem of global warming. Sequestration of CO_2 in aquifers is achieved by the following processes: (1) storage of CO_2 as free-phase gas in the pore spaces (hydrodynamic and capillary trapping), (2) dissolution of CO_2 in the formation water and (3) mineral trapping through geochemical reactions [1–3]. According to Kumar et al. [1], the residence time of the CO_2 in aquifers for sequestration applications is of the order of 10.000 years and different times scales for the different processes must be considered. Dissolution of CO_2 in water is rapid and strongly depends on the contact between the phases, whereas the time scale for trapping of CO_2 as free gas is much longer (the life time of the project) and strongly depends on the reservoir properties. Geochemical reactions (e.g., mineral trapping) are in general very slow, however, under some conditions the rate may be comparable to other transport processes [1].

One of the key-issues considered in CO_2 sequestration are the capillary pressure related properties of porous media. Kumar et al. [1] concluded that capillary trapping of CO_2, i.e., as residual gas or as gas trapped below an internal layer, is the most relevant mechanism for underground storage of CO_2. Other mechanisms for which the capillary pressure behavior is important, are the alternate imbibition and drainage processes in heterogeneous media [4], which results in capillary hysteresis. This non-uniqueness in capillary pressure can be explained by irreversible fluid redistributions [5] and the difference between specific area of the fluid–fluid interface per unit of injected volume [6,7]. For sequestration applications, the hysteresis is of relevance when the fluid displacement leads to residual saturations [1]. Furthermore, capillary pressure is a direct

* Corresponding author. Tel.: +31 15 278 1423.
E-mail addresses: w.j.plug@tudelft.nl (W.-J. Plug), j.bruining@tudelft.nl (J. Bruining).

0309-1708/$ - see front matter © 2007 Elsevier Ltd. All rights reserved.
doi:10.1016/j.advwatres.2007.05.010

measure for wetting effects [8,9]. This wetting behavior is relevant for the integrity of the caprock as a geological seal [1,10]. The seal capacity of the caprock during the project's life time is therefore a measure of the sustainability of CO_2 sequestration. From literature it is found that CO_2 can alter the wettability of the rock [11–13]. These wetting alterations are observed for shaly caprocks by determining the contact angle between brine and CO_2 on a mica and quartz surface [11]. Similar behavior is reported for coal by Siemons et al. [13,14] and Plug et al. [12]. They concluded, from contact angle measurements and capillary pressure data, that the system becomes CO_2-wet near critical conditions.

Therefore, understanding of the capillary pressure behavior is essential in assessing the suitability and potential of CO_2 sequestration in aquifers. In the literature there is a lack of experimental data of capillary pressures for the rock–water–CO_2 systems in the relevant temperature and pressure range. The only reference with data on capillary pressures at relevant conditions are the indirect (relative permeability) measurements reported by Bennion and Bachu [15,16].

For capillary pressure measurements involving CO_2, the complexity of the phase behavior of the CO_2–water system in porous media system requires both sophisticated theoretical and experimental investigations at conditions of practical interest [17–19]. The non-linear behavior for the CO_2 density and viscosity, as function of temperature and pressure [18] in the vicinity of the critical point, is well described by Span and Wagner [20], Duan and Sun [21] and Fenghour et al. [22]. The solubility of CO_2 in water for various pressures and temperatures is experimentally investigated by Wiebe and Gaddy [23] and a thermodynamic description is given by Duan and Sun [21]. Chun and Wilkinson [24] investigated the interfacial tension for CO_2–H_2O mixtures for a wide range of temperatures and pressures. The results showed a minimum for the interfacial tension at the critical point of CO_2. Numerical and analytical models for the prediction of CO_2 sequestration on the long term can be found in the work of Pruess and Garcia [25], Spycher et al. [17], Ebigbo et al. [18], Class et al. [19] and Nordbotten et al. [26]. For the validation and applicability of these models, experimental measurements are needed to provide the essential input parameters.

The literature describes a number of techniques, which in principle can be used to measure the capillary pressure at the relevant pressure and temperature conditions. Most techniques are based on the porous plate technique [27], the micro-pore membrane technique [28,29], mercury drainage experiments [8] and the centrifuge method [30,31]. Conventional capillary pressure studies use the multi-step method, where after a finite pressure increment an equilibrium water saturation distribution is established. Experimental data are also available in the literature where continuous phase injection is applied [32–40]. These experimental data can be considered as quasi-static because small displacement rates are applied.

In this study, we performed capillary pressure measurements on the unconsolidated sand–CO_2–distilled water system up to near critical conditions. The reason we choose to investigate the capillary behavior of unconsolidated samples is because the experimental set-up is not suitable for consolidated cores.

The objective of this work is to develop a method with which static drainage and imbibition capillary pressures for CO_2 can be measured continuously as a function of saturation at various temperature (T) and pressure (P) conditions and to investigate the effects of the dissolution of CO_2 in water during the CO_2 sequestration process. Quasi-static conditions are achieved by applying small injection rates (0.01–0.1PV/h). To understand the influence of the dissolution process for the CO_2 experiments, nitrogen (N_2) experiments are conducted for which the dissolution effects are much smaller.

From the measurements we expect to observe the mass transfer effects of CO_2 on the injection and production curves because the fluid velocities are very small compared to the mass transfer rate. To understand the effects of dissolution on capillary pressure and the cumulative water production, a quasi-1D, fully implicit numerical numerical model is developed. Moreover, the measurement procedure is validated by this model which simulates the drainage experiments. The simulator is based on the upstream finite volume method that incorporates the CO_2–H_2O phase behavior, mass transfer and dissolution of one phase into another. The mathematical model is explained in Appendix A.

2. Experimental design

2.1. Experimental set-up

The equipment is an optimized version of the set-up presented in Plug et al. [41] and Mazumder et al. [42], and is based on the porous plate technique combined with the micro-pore membrane technique, discussed by Jennings et al. [28], Longeron et al. [29] and Christoffersen and Whitson [27]. This set-up is suitable to measure the capillary pressure for water–gas (N_2 and CO_2) system in unconsolidated quartz sand for different fluid pressures (P_{atm} – 85 bar) and temperatures. An overview of the temperature and pressure properties of each experiment performed, are listed in Table 1.

In Fig. 1, the schematic diagram of the set-up is shown and the cross section of the sample holder is shown in Fig. 2 and discussed in Section 2.2. Two syringe pumps (ISCO pump, 260D) are connected to the in- and outlet of the sample holder and can be set to a constant injection rate (accuracy ±0.005 ml/h) or a constant pressure (accuracy ±0.01 bar). The gas phase is injected or produced at the top of the sample holder and the water is collected or injected at the bottom using the water syringe pump for pressures above 1 bar. For primary drainage experiments at atmospheric conditions, valve 7 is closed and valve 8 is open and the water is produced in a beaker placed on a bal-

Table 1
Correlation between the experiment numbers and the experimental properties and conditions

Nr.	Gas	P (bar)	T (°C)	σ[a] (mN/m)	ρ_s (kg/m^3)	V_{helium}[b] (ml)	V_{water} (ml)	φ (–)
1	CO_2	P_{atm}	23	71	No data	No data	No data	0.36
2	CO_2	P_{atm}	21	71	No data	No data	No data	0.34
3	CO_2	P_{atm}	22	71	No data	No data	No data	0.35
4[c]	N_2	P_{atm}	24	71	1660	93.8	92.0	0.37
5	N_2	P_{atm}	27	71	1658	94.4	95.2	0.37
6	CO_2	P_{atm}	24	71	1661	93.8	94.5	0.36
7	CO_2	P_{atm}	26	71	1661	95.6	96.4	0.38
8	CO_2	8	26	68	1657	93.9	93.6	0.37
9	CO_2	8	28	67	1666	93.7	93.3	0.37
10	CO_2	8	28	67	1666	94.1	93.1	0.37
11	N_2	8	27	71	1656	93.1	93.0	0.37
12[c]	CO_2	85	27	30	1656	93.5	93.15	0.37
13[c]	CO_2	85	40	32	1671	91.8	91.3	0.36

[a] Data obtained from Chun and Wilkinson [24].
[b] The average helium volume for five measurements.
[c] Experiments conducted with the stainless steel ring ($H = 25$ mm).

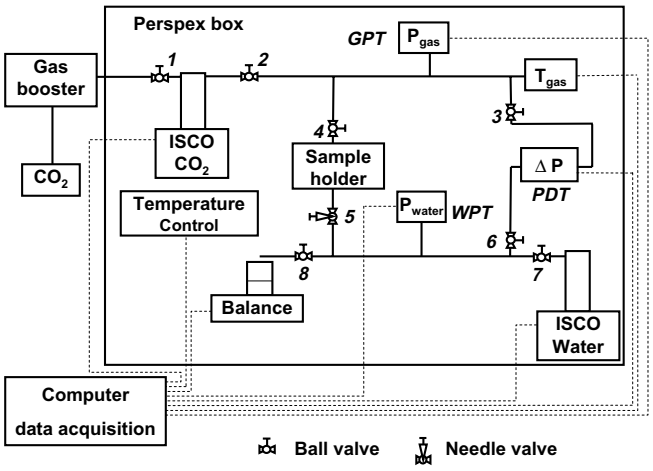

Fig. 1. Schematic lay-out of the experimental set-up.

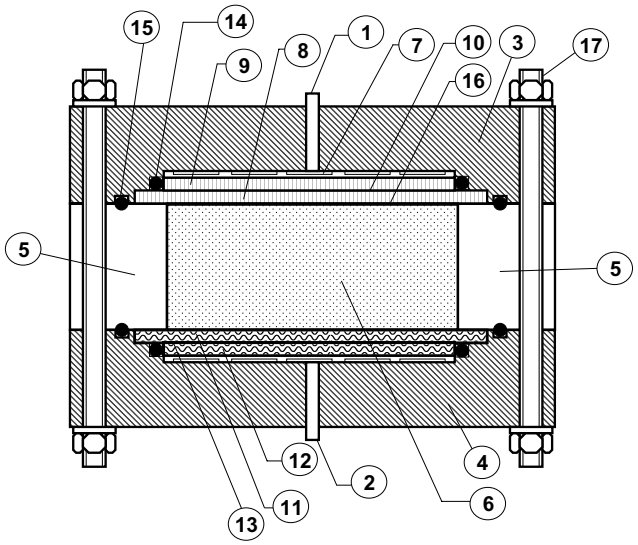

Fig. 2. Cross section of the sample-holder: 1. gas-inlet; 2. water-inlet; 3. stainless steel end-piece 1; 4. stainless steel end-piece 2; 5. stainless steel ring (height $H = 25$ mm); 6. porous medium (diameter, $D_{sample} = 84$ mm); 7. concentric grooves; 8. perforated plate (diameter, $D_{ss,1} = 90$ mm); 9. perforated plate (diameter, $D_{ss,2} = 84$ mm); 10. hydrophobic filter (diameter, $D_w = 90$ mm, pore size, 0.45 μm); 11. SIPERM filter (diameter, $D_{s,1} = 90$ mm); 12. SIPERM filter (diameter, $D_{s,2} = 84$ mm); 13. water-wet filter (diameter, $D_G = 90$ mm, pore size, 0.1 μm); 14. O-rings (2.1 mm); 15. O-rings (4 mm); 16. nylon filter (pore size 210 μm); 17. stainless steel bolts.

ance (accuracy ±0.005 g). A layer of paraffin on top of the water surface avoids evaporation. The gas pressure transducer (GPT) and the water pressure transducer (WPT) record the single phase pressures (range 0–100 bar, accuracy ±0.01 bar). The differential pressure between the gas and the water phase is measured by the pressure difference transducer (PDT, range 0–500 mbar, accuracy ±0.1 mbar), which is located at the same height as the middle of the sample, such that no correction for gravity effects is required.

To maintain a constant temperature we cover the entire set-up with a perspex box, sealed by polystyrene. Inside the box two 60 W light-bulbs, which switch on and off, regulate the temperature in the range between 25–40 ± 0.5 °C. We allow temperature equilibration for at least two days for gaseous and liquid CO_2/N_2 and at least three days for supercritical CO_2.

2.2. The sample holder

The sample holder, as shown in Fig. 2, consists of three parts: two end-pieces and a ring that contains the unconsolidated sample. In this work, two types of rings are used: a stainless steel ring with a height of $H = 25$ mm and a PEEK (polyetheretherketone) ring with a height of $H = 27$ mm [41]. The sand pack with a permeability of $k \approx 2 \times 10^{-10}$ m^2, is kept in place using a combination of plates at the top and bottom of the sample. At the bottom, two porous plates (*SIPERM R*, Cr–Ni-*Steel basis*), with a permeability of 2×10^{-12} m^2 and a porosity of 0.32, support the sample and protect the hydrophilic Millipore membrane used in primary drainage experiments. Two stainless steel plates both with 32

perforations ($D_p = 5$ mm) are used at the top directly above the sample in combination with a nylon filter. Between these plates, a hydrophobic membrane is placed for the primary imbibition process, prohibiting water production. To avoid leakage of gas or water over the hydrophobic or hydrophilic membranes, we seal the outer perimeters with a Viton O-ring. Concentric flow grooves in the end-pieces redistribute the injected and produced phase over the total sample area to avoid preferential flow and fast breakthrough of the injected phase.

2.3. Experimental procedure

At the start of each experiment the set-up is cleaned and the porous plates are dried. The assembly of the sample holder is from the bottom upward. For each experiment we use new Millipore filters and new O-rings. When end-piece 2, the porous plates, the hydrophilic membrane and the O-rings included, and the ring are mounted together, we pour the unconsolidated sample in the sample holder. The sample is vibrated for 10 min to obtain a better packing and similar sample densities, ρ_s (Table 1). The last step in assembling the sample holder is to put end-piece 1, the perforated plates, the hydrophobic filter, the nylon filter and O-rings included, on top of the ring and to close the sample holder. The sample holder is placed in between valves 4 and 5 and the entire system is evacuated for 1 h. During the evacuation, valve 4 is closed.

The next step is to determine the porosity, φ, with helium. Therefore, we measure the void volume of the empty sample holder ($V_{\text{void,empty}}$, situation 1) and the sample holder containing the sand ($V_{\text{void,sample}}$, situation 2). Both volumes and the sample volume are used and φ can be defined as follows:

$$\varphi = 1 - \frac{V_{\text{void,empty}} - V_{\text{void,sample}}}{\frac{1}{4}\pi (D_{\text{sample}})^2 H}. \tag{1}$$

In Eq. (1), $V_{\text{void,empty}}$ and $V_{\text{void,sample}}$ include the void volume between valves 4 and 5, the gas tubing (between valves 1, 3 and 4) and the gas pump (see Fig. 1). In both situations, we start with an initial helium equilibrium pressure, $P_{g,1}$, and after moving the piston of the gas pump upwards, we measure the final equilibrium pressure, $P_{g,2}$. From the difference in gas pump volume, ΔV_{pump}, and the two helium pressures we can determine $V_{\text{void,empty}}$ and $V_{\text{void,sample}}$ from

$$V_{\text{void,empty/sample}} = \frac{P_{g,1}\Delta V_{\text{pump}}}{Z_2\left(\frac{P_{g,2}}{Z_2} - \frac{P_{g,1}}{Z_1}\right)} - V_{\text{pump,2}} - V_{\text{tubing}}, \tag{2}$$

where Z_1 and Z_2 are the compressibilities of helium, $V_{\text{pump,2}}$ is the final gas pump volume and V_{tubing} is the volume of the gas tubing. For both $V_{\text{void,empty}}$ and $V_{\text{void,sample}}$ this procedure is repeated five times and the average volume can be obtained. The average volume of the sample holder filled with sand is denoted as V_{helium} and presented in Table 1. For the sand samples we found a porosity in the range of 0.36–0.38 (Table 1). Subsequently, the total system is again evacuated for 1 h and filled with water from the water pump by closing valve 4 and opening valve 5 (Fig. 1). The values for the water volume, V_{water}, are presented in Table 1. Comparison between V_{helium} and V_{water} shows small deviations ($\sim$1%), which can be explained by systematic measurement errors and the accuracy of the measurement devices. Since we use helium the system is leak-tested before each experiment.

When an experiment starts with the primary drainage process, the hydrophobic filter is left out. This makes it easier to pressurize the system. Due to the high pressure, small air bubbles carried along with the distilled water are dissolved. Similar to the primary drainage process, the hydrophilic filter is removed for primary imbibition tests. In this work, we consider three types of experiments: A. Primary drainage experiments at atmospheric pressure (P_{atm}), B. primary drainage and C. secondary imbibition experiments at pressures above P_{atm}:

(A) The total sample holder is initially filled with water between valve 4 (closed) and valve 5 (see Fig. 1). Subsequently the water pump is used to apply a pressure of 10 bar to remove all possible air and to obtain 100% water saturation. When the pressure becomes 10 bar, the water pump is stopped and valve 7 is closed. Subsequently, valve 8 is opened and the water pressure decreases towards the atmospheric pressure. The gas tubing and the gas pump are filled and flushed with either N_2 or CO_2. Finally, we set a constant temperature and let the system equilibrate for 48 h. The primary drainage experiment starts when a constant gas injection rate is applied and valve 4 is opened. Due to operational restrictions of the ISCO pumps for pressures below 1 bar, no imbibition tests are conducted for atmospheric conditions.

(B) For high pressure experiments the sample holder is initially filled with water and the water pump is set to the fluid pressure we apply during the drainage measurement. Valve 4 is closed and the gas tubing and pump are filled with CO_2 (or N_2). A gas booster, connected to valve 1 (Fig. 1) is used to bring up the gas pressure. We set a constant temperature and let the system equilibrate. Subsequently, when both the water and gas pressure are equal, a constant gas injection rate is applied, the water pump is set to a constant pressure and valve 4 is opened.

(C) After the primary drainage process, the secondary imbibition process starts when the water pump is set to a constant injection rate and the gas pump is set to a constant production pressure.

3. Data analysis procedure

The water saturation (S_w) is obtained by the mass of water produced for the atmospheric conditions and by

the change in volume of the water pump for high pressure conditions ($P > 1$ bar). At the end of the experiment, the integral mass balance is checked by weighing all the separate parts of the sample holder, from which an estimation of the final water saturation in the sample can be obtained.

For the high pressure drainage experiments the amount of water in the pump is measured to validate whether only negligible amounts of 'free' gas are produced. For imbibition tests we apply essentially the same procedure to validate that there is only negligible water production. It turns out that the gas volume in the water pump never exceeds one percent of the volume [28]. The capillary pressure curves are obtained based on the following:

(1) The decrease (increase) in water saturation can be obtained from the mass/volume produced (injected).
(2) The initial water (gas) saturation for primary drainage (imbibition) is 1.
(3) For small injection rates (<1 ml/h), the viscous pressure drop over the sample holder is negligible (~0.04 Pa).
(4) For the drainage experiments all the water from end-piece 1 and the perforated plates is drained before the gas reaches the sample (Fig. 2).
(5) During the drainage process all the water remains in pore space of the SIPERM plates, hydrophilic filter and the void space of end-piece 2 (Fig. 2).
(6) The compressibility of water is neglected for all pressure conditions.
(7) The porosity for all samples used is constant during the drainage and imbibition process.
(8) The capillary pressure is defined as the difference in the gas and water bulk phase pressures and measured by the PDT device.

As an illustration we discuss the procedure to obtain the capillary pressure curve for a primary drainage experiment conducted with a constant CO_2 injection rate at a system pressure of $P = 85$ bar and $T = 27$ °C. Fig. 3 shows the cumulative water production and gas injection data together with P_c as a function of time. The drainage process starts at point A, where the capillary entry pressure is reached. A fast increment in differential pressure, from 0 to 5 mbar is observed and the corresponding cumulative water production and gas injection volume are 12.75 ml and 13.75 ml, respectively. The produced water volume is in agreement with the total void volume of end-piece A. The drainage process ends at point B. At this moment, a steep rise in capillary pressure is observed and the liquid CO_2 attains the SIPERM filter. The cumulative water production and gas injection at this point is 61.67 ml and 63.03 ml, respectively.

The irregularity in the measured P_c is due to the delay in response of the water pump, which is set to a constant production pressure. The water pump measures the pressure with an accuracy of 10 mbar, and consequently, the data consist of a series of spikes, which are not shown in most

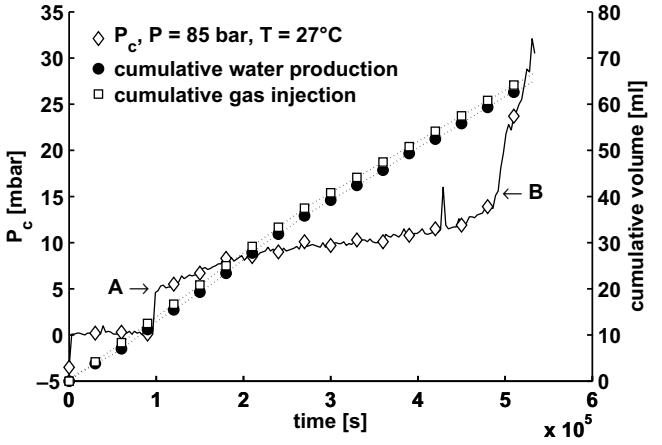

Fig. 3. The drainage capillary pressure, cumulative water production and gas injection (0.5 ml/h) as function of time for CO_2 injection at 85 bar and 27 °C .From these data we obtain the start (A) and end (B) of the primary drainage process. In Fig. 7, the corresponding capillary pressure curve is shown.

of the cases, by plotting only local minima. In some exceptional cases, however, the local minima still show these irregularities. To obtain the P_c–S_w curve, we compute the water saturation from the water production volume using the following expression:

$$S_w(t) = 1 - \frac{V_{wp}(t) - V_{wp}(t_s)}{\varphi V_{sample}}, \tag{3}$$

where V_{wp} is the water pump volume and φV_{sample} is the pore volume of the sample. The corresponding capillary pressure curve (experiment 12) is shown in Fig. 7 and the details of this measurement are further discussed in Section 4.2.

4. Experimental results

In this section, the experimental results are presented for the unconsolidated sand–CO_2–water system. Nitrogen (N_2) experiments are performed to facilitate the interpretation of the CO_2 experiments with the strong dissolution effects. We also describe the repeatability of the experimental method and the effects of different sand packs used. To clarify the correlation between the experiments and the numbering, an overview of the sample and system properties applied during the experiments is given in Table 1.

4.1. Experimental results at atmospheric pressures

To assess the repeatability of the experimental method and of the way we construct the unconsolidated porous medium, we have conducted three primary drainage experiments for three different sand packs, using fine unconsolidated sand with an average particle size of $160 < D_{50} < 210$ μm. For the intermediate water saturation range ($0.4 < S_w < 0.8$) the capillary pressure curves are repeatable with a deviation in P_c of ±1.5 mbar. The

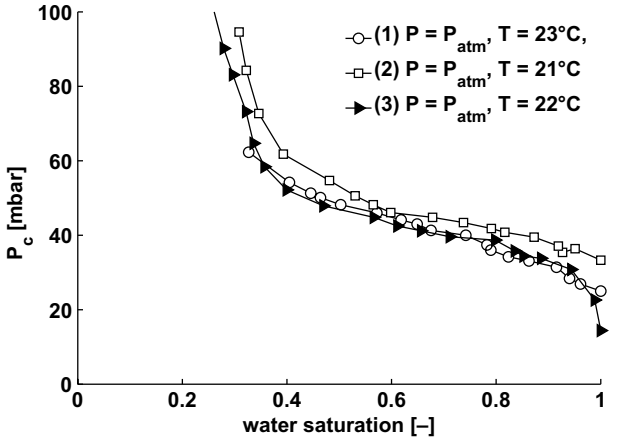

Fig. 4. Primary drainage capillary pressure curves for CO_2 injection in fine sand ($160 < D_{50} < 210$ μm) for atmospheric conditions. In each case the CO_2 injection rate is 0.5 ml/h. The differences observed are an indication of the repeatability of the experimental method.

repeatability slightly decreases near the end point saturations (P_c ±3 mbar).

The second series of experiments at atmospheric conditions is performed on four different coarse sand packs with an average grain size range of $360 < D_{50} < 410$ μm. This coarse sand is also used for high pressures measurements ($P > P_{atm}$). We apply gas injection rates of $u_{inj} < 0.02PV/$h, and therefore, we can assume that the P_c–S_w curves are obtained under quasi-static conditions (see assumption 3, Section 3). Two primary drainage curves are measured with N_2 (experiments 4 and 5) and two with CO_2 (experiments 6 and 7). The results for the primary drainage curves are presented in Fig. 5. The differences in capillary pressures are mainly due to different sand packing and temperature conditions. Indeed, the P_c–S_w curves show the repeatability of the experimental method and the results

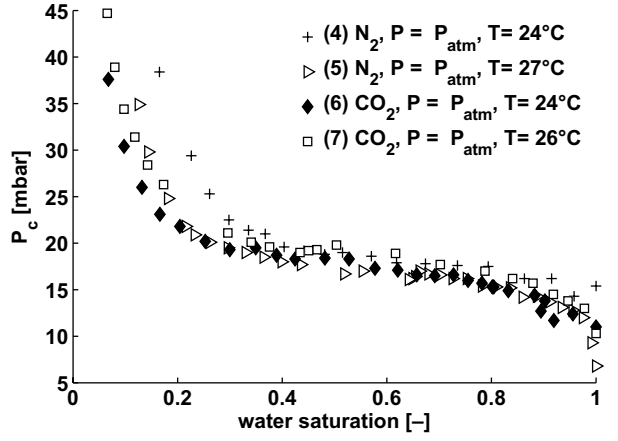

Fig. 5. Primary drainage capillary pressure curves for N_2 and CO_2 injection at atmospheric conditions. The capillary pressure for both gasses are in the same range due to similar interfacial tensions. For experiment 4, S_{wc} is higher compared to the other experiments. This is a result of the relatively high injection rate, $u_{inj} = 2$ ml/h, applied for the saturation range between 0.18 and 0.27.

are within the precision of the experimental method (see Fig. 4). The peak at $S_w = 0.5$ (experiment 6) is attributed to an experimental artifact. A difference in residual water saturation (S_{wc}) is observed between the CO_2 drainage and N_2 drainage experiments. Comparing both the N_2 experiments, S_{wc} is 0.16 and 0.11 for experiments 4 and 5, respectively. In the case we use CO_2, the difference in residual water saturation is much smaller, $S_{wc} = 0.06$ and $S_{wc} = 0.08$ for experiments 6 and 7, respectively. Finally, from Fig. 5 we observe that the drainage curves of the N_2–water system and the CO_2–water system are slightly different, but in the same range. This can be explained by the small difference in interfacial tension between CO_2 and N_2 (see Table 1).

4.2. Experimental results at high pressures, $P > 1$ bar

The P_c–S_w relationships for the coarse sand sample are investigated at conditions of practical interests. Applying different pressure and temperature conditions we can compare the capillary pressure behavior for different interfacial tensions of CO_2 (Table 1), which will result in a pressure dependent capillary pressure. Moreover, the effect of the dissolution of carbon dioxide into the water phase as function of the fluid pressure can be determined by comparing the CO_2 and N_2 capillary pressure curves.

For the 8 bar conditions we performed three measurements with CO_2 and one with N_2. The primary drainage and secondary imbibition curves for experiments 8–11 are presented in Fig. 6. In these four measurements the boundary conditions are such that the gas pressure is set to a constant pressure during the total capillary cycle. Consequently, the water pump is set to a refill rate of 0.5 ml/h. Except at low water saturations the reproducibility for both the drainage and imbibition processes appears to be excellent, considering the different sand packs [41]. The small irregularities at high water saturations for the secondary imbibition experiment (experiment 9, Fig. 6) are attributed to summer temperatures in the laboratory, exceeding the upper limit of the temperature control system. For the primary drainage experiment 10 (Fig. 6) there are no data points between $0.85 < S_w < 0.95$. For both the secondary imbibition experiments 9 and 10, the residual gas saturation is determined at $S_w = 0.92$. Different sand packing combined with the lower temperature (26 °C for 8 and 28 °C for 9 and 10) result in a small deviation for the saturation range of $0.15 < S_w < 0.5$ and a lower residual gas saturation of $S_{gr} = 0.02$.

From Fig. 6, it is clear that the N_2 injection test shows drainage and imbibition capillary pressures similar to the CO_2 measurements. However, as a consequence of different dissolution properties between N_2 and CO_2 the residual gas saturation with N_2 is higher than for CO_2, where S_{gr} for N_2 is 0.21.

In Fig. 7, the results are presented for measurements performed at system pressures above 80 bars. Experiment 12 is conducted with liquid CO_2 ($T = 27$ °C) and supercrit-

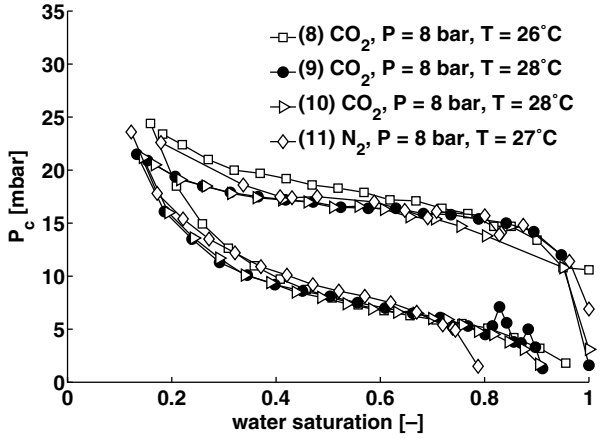

Fig. 6. P_c–S_w primary drainage (upper curves) and secondary imbibition curves (lower curves) at 8 bar, for experiments 8–11 obtained for the coarse sand sample with CO_2 and N_2 and a flow rate of 0.5 ml/h. The reproducibility of the experiment is excellent.

ical conditions are applied for experiment 13 ($T = 40$ °C). It can be seen that the drainage capillary pressure for liquid CO_2 and supercritical CO_2 is of the same range. For the supercritical situation the primary drainage shows significant irregular behavior as a result of sudden imbibition events, whereas for the liquid CO_2 conditions a smooth P_c–S_w curve is measured. The secondary imbibition curve shows negative capillary pressure values for $S_w > 0.5$ (Fig. 7).

To show the pressure dependence of the capillary pressure for drainage, we compare in Fig. 8 the primary drainage curves for CO_2 pressures of 1, 8 and 85 bar. The secondary imbibition curves for experiments 8, 10 and 13 are compared in Fig. 9. For both the primary drainage and the secondary imbibition a decrease in capillary pressure is measured for increasing CO_2 pressures. The pressure dependence of the drainage capillary pressure is a result of the interfacial tension [24] (Table 1). Hence, the capillary pressure curves can be scaled according to the interfacial tension, as shown in Fig. 10. Here, P_c/σ is plotted as function of S_w and small deviations between the three pressure conditions are observed. Contrary to the drainage curves, the secondary imbibition curves cannot be properly scaled by the interfacial tension. In Fig. 11, we show that the values of P_c/σ for supercritical conditions are much smaller than for gaseous CO_2 ($P = 8$ bar), implying that other mechanisms influence the capillary pressure at high pressures and temperatures. This will be further discussed in Section 5.

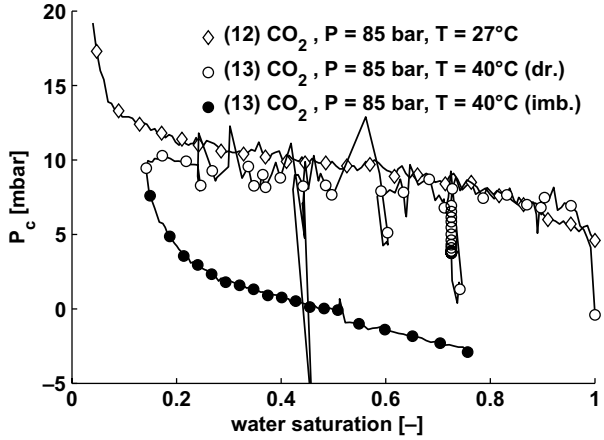

Fig. 7. Primary drainage capillary pressure curves for liquid (◊) and supercritical CO_2 (○). The irregularities observed for experiment 13 are due to imbibition events and temporarily CO_2-wet behavior. The secondary imbibition curve for supercritical conditions is represented by the closed circles (●). Note that for experiment 13 the capillary pressure becomes negative for $S_w > 0.5$.

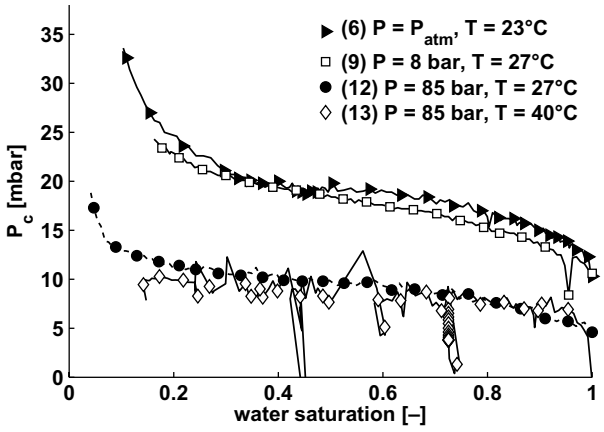

Fig. 8. Primary drainage capillary pressure curves for CO_2 injection in coarse sand at various pressure and temperature conditions. Varying CO_2 injection rates, $\leqslant 1$ ml/h are applied in experiment 6. The CO_2 injection rate is 0.5 ml/h for experiments 12 and 13. In experiment 9, the water extraction rate is 0.5 ml/h. The differences between the low and high pressure capillary pressure curves are explained by the decrease in interfacial tension for increasing CO_2 pressures (see also Fig. 10).

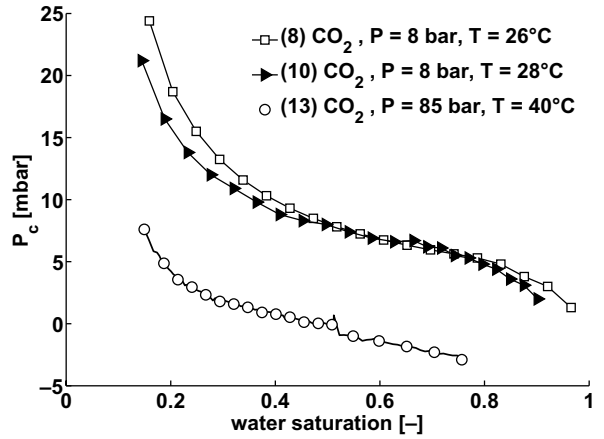

Fig. 9. Secondary imbibition capillary pressure curves for the CO_2–water system in coarse sand for gaseous CO_2 (experiments 8 and 10) and supercritical CO_2 (experiment 13). The water injection rate is 0.5 ml/h for all experiments. The differences between the low and high pressure capillary pressure curves are explained by wetting alteration (see also Fig. 11).

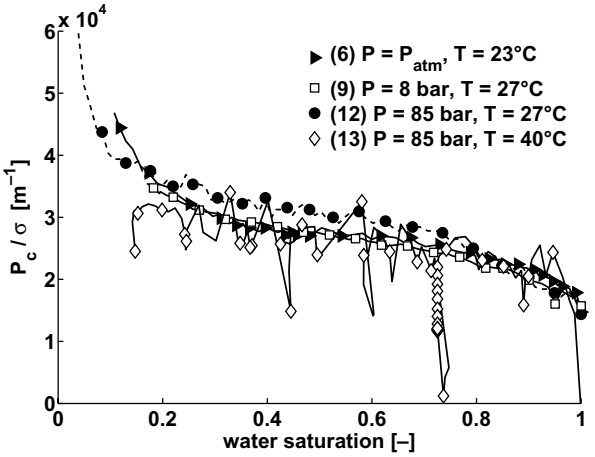

Fig. 10. Primary drainage capillary pressure scaled by the interfacial tension (P_c/σ) for different CO_2 pressures. The interfacial tensions are obtained by Chun and Wilkinson [24] and are listed in Table 1. Small deviations are observed.

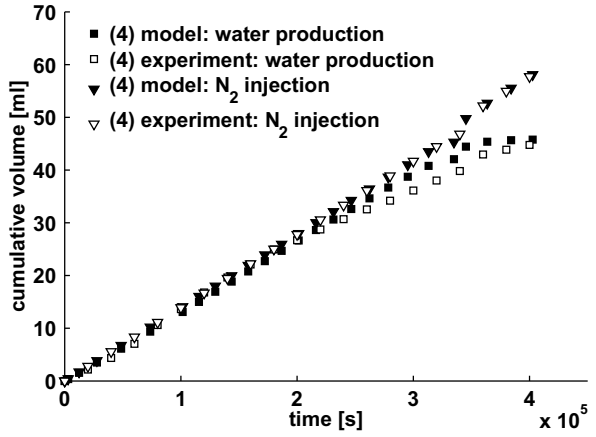

Fig. 12. Experimental and numerical results for the cumulative water production and N_2 injection volume during primary drainage for experiment 4 ($u_{inj} = 0.5$ ml/h, $P = P_{atm}$, $T = 24$ °C). The experimental results are well predicted by the numerical model. Due to the low solubility of N_2 in water, the production and injection curves coincide for $t < 3 \times 10^5$ s. The discrepancy near S_{wc} is explained by viscous forces.

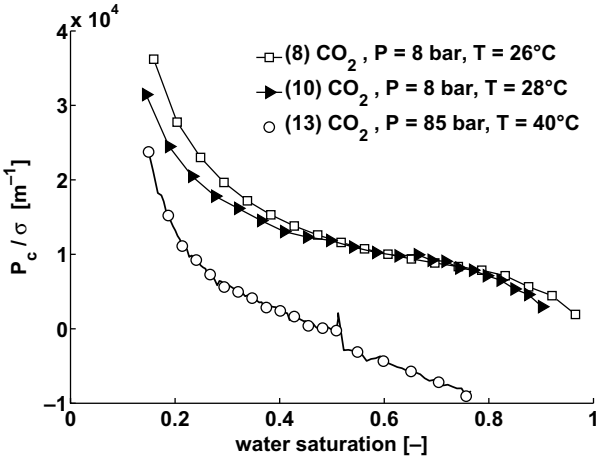

Fig. 11. Secondary imbibition capillary pressure scaled by the interfacial tension (P_c/σ) for gaseous CO_2 (experiments 8 and 10) and supercritical CO_2 (experiment 13). The significant difference between the gaseous and supercritical curve is a result of wetting alteration due to increasing contact angles [11] (see also Fig. 9).

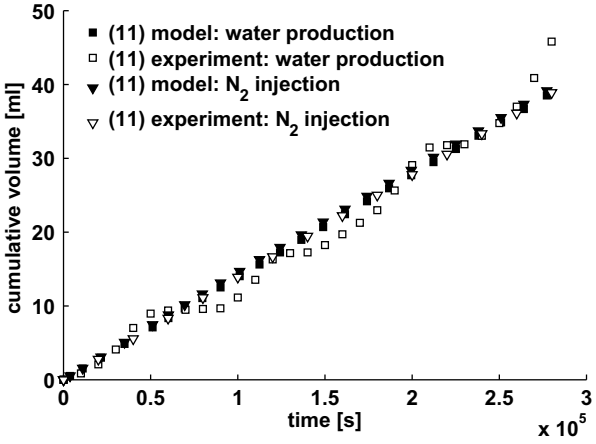

Fig. 13. Experimental and numerical results for the cumulative water production and N_2 injection volume during primary drainage for experiment 11 ($P = 8$ bar, $T = 27$ °C). Good agreement is found between the experimental and numerical results and the production and injection curves coincide, as a result of the insignificant mass transfer between N_2 and water.

4.3. Production and injection behavior during primary drainage

In this section, we describe the results obtained for the injection and production behavior of five primary drainage experiments. Figs. 12 and 13 show the cumulative water production and gas injection for N_2 at atmospheric pressure (experiment 4) and 8 bar (experiment 11), respectively. For both experiments the N_2 injection rate is 0.5 ml/h. At $t = 3.4 \times 10^5$ s the gas injection rate is changed from 0.5 ml/h to 2 ml/h for experiment 4. During the measurements with N_2, the injected and produced cumulative volumes are similar. A discrepancy between the water production and gas injection volumes for the atmospheric condition is observed near S_{wc}, which can be explained by viscous forces. For the high pressure N_2 case (8 bar), the measured water production shows an irregular behavior, which is attributed to temperature effects.

The production and injection curves for primary drainage experiments with CO_2 are presented in Figs 14–16. The differences between the injected and produced volumes for the atmospheric case (Fig. 14) and the 8 bar experiment (Fig. 15) can be explained by the dissolution effects of CO_2 in water (Section 5). When liquid CO_2 is injected (Fig. 16) these effects are not observed and the cumulative gas volume injected is almost equal to the cumulative water volume produced.

The details of the measured injection and production curves for both N_2 and CO_2 are compared with the numerical results and are further discussed in the next section.

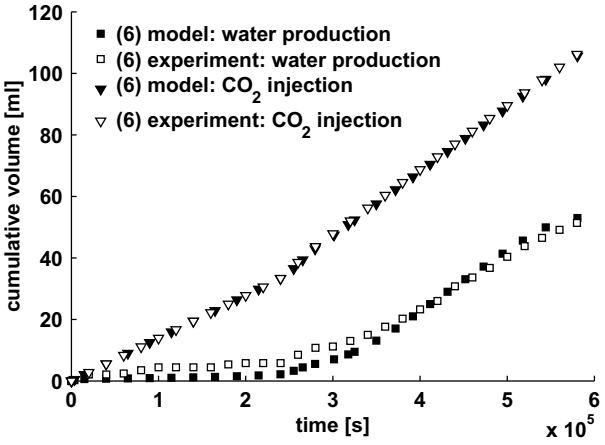

Fig. 14. The cumulative water production and CO_2 injection volume during primary drainage for experiment 6 at atmospheric conditions and $T = 24$ °C. Good agreement is found between the experimental and numerical results. As a result of the dissolution of CO_2 in water, the production and injection curves deviate significantly and the water production starts to increase after the water is saturated with CO_2.

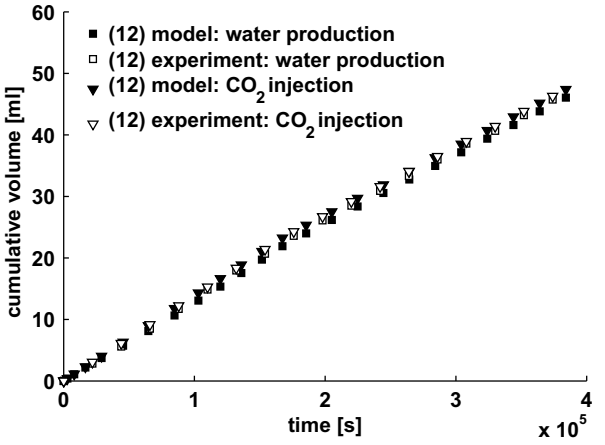

Fig. 16. Experimental and numerical results for the cumulative water production and liquid CO_2 injection volume ($P = 85$ bar, $T = 27$ °C). Good agreement is found between the experimental and numerical results. Although the CO_2 will dissolve in the water, the production and injection curve coincide because the mass transfer of CO_2 barely influences the CO_2 pressure.

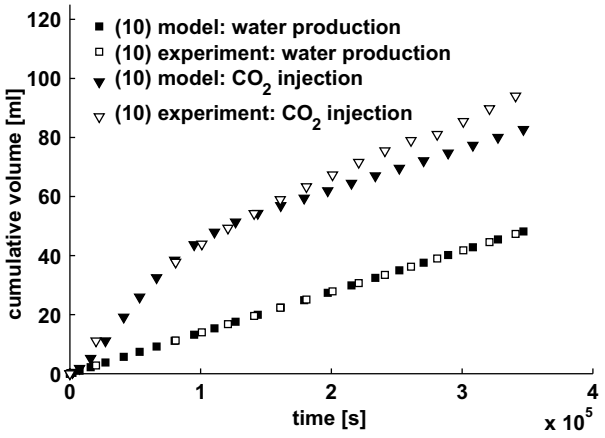

Fig. 15. The cumulative water production and CO_2 injection volume during primary drainage for experiment 10 at 8 bar and $T = 28$ °C. Good agreement is found between the experimental and numerical results for $t < 1.5 \times 10^5$ s. The CO_2 mass transfer is observed and results in a difference between the production and injection volumes. The discrepancy between the model and experimental results can be explained by CO_2 diffusion in water from the sample to the water production pump.

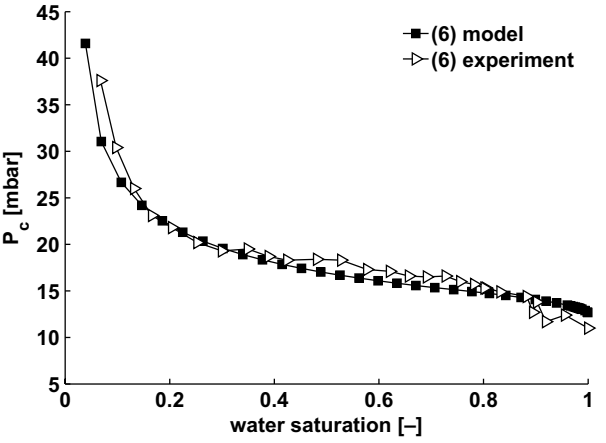

Fig. 17. Primary drainage capillary pressure curves, measured and predicted for CO_2 injection at atmospheric conditions (experiment 6). The CO_2 injection rate is 0.5 ml/h. The numerical results are computed from Eq. (A.18) and good agreement is found with the measured P_c–S_w curve.

5. Discussion

To get a better understanding of the different processes and mechanisms observed in the experiments, we have developed a one-dimensional, fully implicit flow simulator. The model equations are derived in Appendix A and the model input parameters are presented in Table A.1.

Fig. 17 plots the experimentally and the numerically obtained P_c–S_w curves for the CO_2–water system at atmospheric conditions (experiment 6). It is clear that the measured capillary pressure curve shows good agreement with the predicted capillary pressure curve, based on the bulk gas and water pressure (see Eq. (A.18)). This indicates that the experimental method is validated by the numerical model and that the assumptions, listed in Section 3 are justified. Small discrepancies between the measured and predicted curves near the end point saturations are a result of the input capillary pressure curve, based on the Leverett-J function (see Eq. (A.8), Appendix A.3). Moreover, the numerical simulations show that the SIPERM plates at the bottom have no effect on the measured P_c–S_w curve for the flow conditions applied. Indeed, it can be expected that for viscous dominated displacement, i.e., higher injection rates, the effects of the SIPERM plates on P_c are observed [43].

The small values for S_{wc} measured for low and high pressure primary drainage experiments with CO_2 can be

explained by the quasi-static conditions. For the small injection rates, the displacement is capillarily dominated ($Ca \sim 10^{-8}$) and entrapment of water plays a minor role [38]. For the drainage process with N_2, experiment 4 in Fig. 5, we conclude that the exceptional high gas injection rate applied near S_{wc} (2 ml/h) causes more hydraulic isolation of water filled pores [38]. Hence the water phase becomes more disconnected and viscous forces start to dominate for higher saturations [40]. An increase in S_{wc} compared to the other experiments is than observed. This behavior is also predicted by the model, where near S_{wc} the production of water tends to zero and a fast increment in P_c is computed (e.g., Fig. 12).

Differences in S_{gr} between CO_2 and N_2 imbibition experiments (Fig. 6) are a result of the dissolution behavior of CO_2. This effect is observed in experiment 10 where water breakthrough occurs for almost one day and a reasonable amount of water is produced (12.4 ml). After we start the secondary drainage experiment (not shown here), the volumetric water balance is derived, and only 9 ml of water is produced before the increment of P_c is observed (similar to event A in Fig. 3). Under the assumptions that no water remains in the stainless steel filters and the gas tubing (see Fig. 2) and $\frac{c_{ww}}{c_{wW}} \approx 1$ (Eq. (A.13)), the water saturation at the start of the secondary drainage process approximates $S_w = 1$. This indicates that the total amount of residual CO_2, present at the moment of water breakthrough after imbibition, has been dissolved in the water. Therefore, we assume that the water phase is not fully saturated with CO_2 at the end of the imbibition process.

One of the objectives of this work is to provide experimental data for the capillary pressure, measured for the rock–water–CO_2 systems in the relevant temperature and pressure range, e.g., experiments 12 and 13 (Fig. 7). The only reference with data on capillary pressures with which we can compare our results are the measurements reported by Bennion and Bachu [16]. They reported on positive drainage capillary pressures for the supercritical CO_2–brine systems, ranging from 0.1 ($S_w = 1$) to 1000 bar ($S_w = S_{wc}$). However, these capillary pressures were obtained from indirect measurements (relative permeability) and for low permeable cores (2.1×10^{-14} m^2).

The complex behavior of the CO_2–water system is observed during supercritical displacement (experiment 13, Fig. 7) and is explained by phase instabilities in the vicinity of the critical point. Small system perturbations, like temperature variations and corresponding thermal expansion effects, will cause density and viscosity changes. This results in occasional water imbibition during continuous CO_2 injection (observed as fast drops in P_c). In addition, temporary CO_2-wet conditions are considered. Because the CO_2 trapped in the crevices of the sand will not instantaneously dissolve in the water, the water will 'see' a surface consisting of sand and gas patches.

The negative secondary imbibition capillary pressures, measured for $S_w > 0.5$ (Fig. 9), indicates that the CO_2–water–sand system becomes intermediate wet. Chiquet et al. [11] already concluded that the wettability of minerals, such as quartz, can be significantly altered in the presence of CO_2 under typical sequestration conditions. For these high pressures and temperatures, the solvent properties of CO_2 improve and together with the decrease of pH of water, the surface charges become less negative. This will reduce the electrostatic interfacial forces that favor positive capillary pressures. In addition to this, the contact angle increases for supercritical conditions. This is shown in Fig. 11, from which it is clear that imbibition capillary pressure does not scale with the interfacial tension.

To obtain a correct interpretation of the diffusion and dissolution mechanisms, and their impact on the capillary pressure, the experimental results for the water production and the gas injection behavior are compared to the model predictions. From the numerical simulations it appears that the results in cumulative volumes are independent of the discretization (Fig. 18). The injection and production characteristics for the primary drainage experiments with N_2 and CO_2 are presented in Figs. 12–16. Good agreement between the predicted and measured volumes is found for both the low and high pressure conditions. For the 8 bar N_2 experiment (Fig. 13), the measured water production curve is on average a straight line, which is also predicted by the model. Due to the low solubility of N_2 in water ($k_H \approx 8 \times 10^9$ Pa), the mass transfer rate, defined by the right hand side of Eq. (A.2), does not have a significant effect on the water production curves.

Contrary to the experiments with N_2, the dissolution rate and the diffusion of CO_2 in water influence the water production profiles for $P = P_{atm}$ and $P = 8$ bar (see Figs. 14 and 15). The water production during CO_2 injection at atmospheric conditions (Fig. 14) is initiated very slowly (stage 1) because the CO_2 dissolves into the water and the process is dominated by diffusion. The duration of stage 1 corresponds to the characteristic diffusion time, defined by

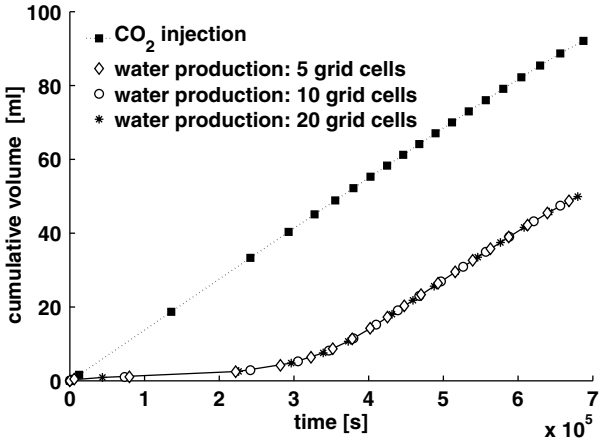

Fig. 18. Numerical computations for CO_2 injection at atmospheric conditions for three different discretizations. As input parameters we use: $u_{g,inj} = 0.5$ ml/h, $D_L = 1 \times 10^{-2}$ m, $T = 28$ °C and the capillary pressure data from experiment 6 (see Table A.1). No effect of the grid size on the water production behavior is computed.

$t_c = H^2/D_g$. Because the water saturation does not decrease significantly, we assume H (the water column in the sample) to be constant during stage 1. For constant H and $D_g = 2 \times 10^{-9}$ m^2/s [44], $t_c \approx 3$ days. For $t > t_c$, the gas pressure starts to build up and the water production increases (stage 2). Subsequently, the production curve becomes parallel to the gas injection profile, until S_{wc} has reached (stage 3). From this moment the water production is almost horizontal (stage 4).

For the 8 bar CO_2 experiment, (Fig. 15), different boundary conditions were applied ($P_{g,z=0} = $ constant, $u_{w,z=-L} = $ constant). The constant water production is indicated by the constant slope. Similar to the atmospheric case (experiment 6) the gas injection curve is subject to the CO_2 dissolution rate in the first stage of the experiment, $t < 1.2 \times 10^5$ s. As a result of the constant water production, the water column in the sample decreases, which results in a smaller t_c. The model predicts similar behavior as observed during the measurement. However, a discrepancy in cumulative gas production is found between the simulated and measured data after $t \approx 1.5 \times 10^5$ s. This results in an underestimation of the predicted cumulative CO_2 volume at the end of 12.2 ml.

For the liquid CO_2 case (Fig. 16) the dissolution and diffusion effects do not influence the water production behavior, and both the experimental and numerical results show an incompressible-like displacement. Because $c_{gg} \gg c_{wg}^{eq}$ (Eq. (A.2) and Eq. (A.13)), the influence of the mass transfer on the CO_2 pressure, is negligible. Here, c_{gg} is the concentration of CO_2 in the liquid CO_2 phase. Comparison of experiment 12 with experiments 6 and 10, shows that the solubility of gaseous CO_2 is relatively smaller than for liquid CO_2 [21]. A small deviation in cumulative production and injection of approximately 1 ml is found over the period $t < 4 \times 10^5$ s. Different mass transfer rates are investigated for the liquid CO_2 conditions, and indeed, no effect on the water production profiles is predicted.

The comparison between the gaseous CO_2 and N_2 experiments shows the large effect of the dissolution of CO_2 on the injection/production behavior. However, the capillary pressure is not influenced by dissolution effects, because the capillary pressure curves obtained for the CO_2–water and N_2–water system (Figs. 5 and 6) are all in the same range.

6. Conclusions

(1) A capillary pressure set-up has been developed and validated that can be used to measure the capillary pressure behavior for CO_2 sequestration applications.
(2) For the small injection rates applied, the viscous forces are negligible and the capillary pressure curves are considered as static.
(3) The numerical results show that the SIPERM filters do not influence the measured P_c–S_w curves for the applied flow conditions.
(4) Increasing CO_2 pressures result in decreasing primary drainage capillary pressures for all samples used. This can be explained by the decrease in interfacial tension [24].
(5) From the comparison between the N_2 and CO_2 experiments, we conclude that the capillary pressure is not influenced by the dissolution of CO_2 in water.
(6) Measurements close to the critical point of CO_2 show alternate drainage and imbibition events during CO_2 injection. This is a result of small perturbations that change the density and viscosity of CO_2 and temporary CO_2-wet behavior.
(7) The wettability of the quartz sand is altered to intermediate wet in the presence of CO_2 under supercritical conditions. This is a result of improving solvent properties of CO_2 and the decreasing pH of water [11].
(8) Good agreement is found between the experimental results and the model prediction for both the CO_2 and N_2 injection drainage experiments.
(9) The model shows that the water production and gas injection behavior depends largely on mass transfer rate and diffusion of CO_2 in water. These effects become negligible for the injection of liquid CO_2.
(10) The capillary pressure behavior must be considered in CO_2 sequestration application, e.g., the caprock integrity [11] and drainage and imbibition events in heterogeneous rocks [9]. Our measurements show that wetting alteration and the abrupt phase changes and accompanying density and viscosity changes may effect the success of CO_2 sequestration.

Acknowledgements

The research presented in this work was carried out as part of the CATO program: CO_2 Capture, Transport and Storage in the Netherlands (http://www.CO2-cato.nl/). The financial support is gratefully acknowledged. We thank A. Hoving, L. Vogt, P.S.A. de Vreede and H.G. van Asten for technical support.

Appendix A. Numerical model for the unconsolidated sand–water–CO_2 system

We consider the injection of CO_2 and N_2 in a cylindric unconsolidated sample, originally filled with water. The sample consists of unconsolidated sand with constant porosity, φ and permeability, k. The sample is vertical, with a height H and a diameter $D_{inner} = 84$ mm. The gas inlet is at the top of the sample at $z = 0$ and the water outlet is positioned at $z = -L$ and gravity is taken into account.

In Table A.1, the model input parameters are presented which are used in the simulations. Furthermore, the summaries of physical input parameters and variables are given in Tables A.2 and A.3.

A.1. Model equations of the mathematical model

The conservation of mass of each component in each phase is given by the following equations, which express the liquid water mass balance (Eq. (A.1)), the gas mass balance in the gaseous phase (Eq. (A.2)) and the combined gas mass balance in the liquid water and the water vapor in the gaseous phase (Eq. (A.3))

$$\varphi\frac{\partial}{\partial t}(S_{\mathrm{w}}c_{\mathrm{wg}})+\frac{\partial u_{\mathrm{w}}c_{\mathrm{wg}}}{\partial z}-D_{\mathrm{g}}\frac{\partial^2 c_{\mathrm{wg}}}{\partial z^2}=-q_{\mathrm{g}\to\mathrm{g,w}}, \tag{A.1}$$

$$\varphi\frac{\partial}{\partial t}(S_{\mathrm{g}}c_{\mathrm{gg}})+\frac{\partial u_{\mathrm{g}}c_{\mathrm{gg}}}{\partial z}=q_{\mathrm{g}\to\mathrm{g,w}}, \tag{A.2}$$

$$\varphi\frac{\partial}{\partial t}(S_{\mathrm{g}}c_{\mathrm{gw}})+\frac{\partial u_{\mathrm{g}}c_{\mathrm{gw}}}{\partial z}+\varphi\frac{\partial}{\partial t}(S_{\mathrm{w}}c_{\mathrm{ww}})+\frac{\partial u_{\mathrm{w}}c_{\mathrm{ww}}}{\partial z}=0. \tag{A.3}$$

In these equations S_{w} is the water saturation and S_{g} is the gas saturation. Furthermore, u_{w} and u_{g} is the Darcy velocity of the water and the gas respectively and $q_{\mathrm{g}\to\mathrm{g,w}}$ is the mass transfer between the gas phase and the liquid water (Eq. (A.9)). The component concentration is denoted by $c_{\alpha j}$, where α denotes the phase ($\alpha=\mathrm{w,g}$) and j is the component ($j=\mathrm{w,g}$). This system of equations is solved for S_{w}, P_{g} and c_{wg} using the relationships described in Appendix A.3.

A.2. Model assumptions

The following model assumptions for the quasi-1D model are made:

(1) The temperature is constant over the experimental time.
(2) For the initial condition, an equilibrium water saturation is present such that the gas and water velocities are zero.
(3) Only vertical flow is considered.
(4) For the drainage process gas is injected as pure gas.
(5) Two components are present in the sample: the water (w), and gas (g) component.
(6) For N_2 the ideal gas law is used and for CO_2 the Span and Wagner EOS [20] is used.
(7) Thermodynamic equilibrium between the water component in the water and gas phase is considered.
(8) The volume of water and gas are additive, i.e., there is no volume contraction upon mixing.
(9) Mass transfer for the gas component in the gas and water phase is considered.
(10) No interaction between the solid and mobile phases is taken into account.
(11) The water and the rock are incompressible.

A.3. Constitutive relationships

The volumetric flux of phase α is given by Darcy's law, which reads

$$u_\alpha=-\frac{kk_{\mathrm{r}\alpha}}{\mu_\alpha}\left(\frac{\partial P_\alpha}{\partial z}-\rho_\alpha g\right). \tag{A.4}$$

In Eq. (A.4), the viscosity of the gas component, μ_{g} is a function of P and T (Table A.3) and the water viscosity, μ_{w} is a function of T (Eq. (A.20)). The phase pressures and densities are denoted by P_α and ρ_α (Table A.3), respectively. The absolute permeability, k, is obtained from the Carman–Kozeny relation, given by

$$k=\frac{1}{150}(D_{50})^2\frac{\varphi^3}{(1-\varphi)^2}, \tag{A.5}$$

where φ and D_{50} (Table A.1) are respectively the sample porosity and the average grain size. The relative permeability functions k_{rw} and k_{rg} are given by the Brooks–Corey functions:

$$\begin{aligned}k_{\mathrm{rw}}&=k'_{\mathrm{rw}}(S_{\mathrm{we}})^{\frac{2}{\lambda_{\mathrm{s}}}+3},\\ k_{\mathrm{rg}}&=k'_{\mathrm{rg}}(1-S_{\mathrm{we}})^2\left(1-(S_{\mathrm{we}})^{\frac{2}{\lambda_{\mathrm{s}}}+1}\right).\end{aligned} \tag{A.6}$$

Here the effective water saturation, S_{we}, is defined as

$$S_{\mathrm{we}}=\frac{S_{\mathrm{w}}-S_{\mathrm{wc}}}{1-S_{\mathrm{wc}}}. \tag{A.7}$$

The capillary pressure is defined as $P_{\mathrm{c}}=P_{\mathrm{g}}-P_{\mathrm{w}}$, and derived from the Leverett-J function,

$$P_{\mathrm{c}}(S_{\mathrm{w}})=\gamma\sigma\sqrt{\frac{\varphi}{k}}\left(\frac{\frac{1}{2}-S_{\mathrm{wc}}}{1-S_{\mathrm{wc}}}\right)^{\frac{1}{\lambda_{\mathrm{s}}}}\left(\frac{S_{\mathrm{w}}-S_{\mathrm{wc}}}{1-S_{\mathrm{wc}}}\right)^{-\frac{1}{\lambda_{\mathrm{s}}}}, \tag{A.8}$$

where the interfacial tension and the residual water saturation are respectively denoted by σ and S_{wc} (Table A.1). For N_2 it is assumed that σ does not vary for the pressure range from 1 to 10 bar and for CO_2 the interfacial tension changes as function of pressure and temperature. During the simulation, σ for N_2 and CO_2 remains constant.

The dissolution rate of gas in water, $q_{\mathrm{g}\to\mathrm{g,w}}$ (Eqs. (A.1) and (A.2)), is a function of the gas saturation, S_{g}, the actual gas concentration in the water, c_{wg}, and the equilibrium gas concentration in the water, $c_{\mathrm{wg}}^{\mathrm{eq}}$, and is defined by

$$q_{\mathrm{g}\to\mathrm{g,w}}=k_{\mathrm{L}}S_{\mathrm{g}}(c_{\mathrm{wg}}-c_{\mathrm{wg}}^{\mathrm{eq}}), \tag{A.9}$$

where k_{L} is the mass transfer for the dissolution of gas in the water defined by Bird et al. [45]

$$k_{\mathrm{L}}=D_{\mathrm{g}}\frac{12\varphi}{(D_{\mathrm{L}})^2}. \tag{A.10}$$

Here D_{g} is the diffusion coefficient of the gas in liquid water as function of T [44] and D_{L} is the characteristic length of the bubble size. We determine the equilibrium concentration of the gas in the liquid water, $c_{\mathrm{wg}}^{\mathrm{eq}}$, from Henry's law, given by

$$P_{\mathrm{g}}=K_{\mathrm{Henry}}x_{\mathrm{gw}}. \tag{A.11}$$

The Henry's constant is denoted by K_{Henry} and $x_{\mathrm{CO_2}}$ is the molar fraction, defined as

$$x_{CO_2} = \frac{c_{wg}^{eq}}{c_{ww} + c_{wg}^{eq}}. \tag{A.12}$$

Since ideal mixing [46] is assumed in this work, and enthalpy changes due to mixing of the components are zero, the volumes of the components are additive

$$\begin{aligned} \frac{c_{ww}}{c_{wW}} + \frac{c_{wg}}{c_{wG}} &= 1, \\ \frac{c_{gw}}{c_{gW}} + \frac{c_{gg}}{c_{gG}} &= 1, \end{aligned} \tag{A.13}$$

where subscripts W and G indicate the concentrations of the pure components. Both N_2 and vapor water are assumed to behave as an ideal gas, whereas for CO_2 non-ideal behavior is assumed (Eq. (A.16)). The ideal gas law is given by

$$PV = nRT \tag{A.14}$$

and the pure concentrations of water and N_2 can therefore be written as

$$c_{gW} = \frac{P_g}{RT}, \quad c_{gG} = \frac{P_g}{RT}, \tag{A.15}$$

where P_g is the total gas pressure and R is the universal gas constant. For CO_2 we use the Span and Wagner equation of state [20] and the pure CO_2 component can be written as

$$c_{gG} = \frac{P}{z(P,T)RT}, \tag{A.16}$$

where $z(P,T)$ is the gas compressibility of CO_2. From Eq. (A.13), c_{gw} is determined from

$$c_{gw} = \frac{P_{w,sat}}{RT}, \tag{A.17}$$

where the water vapor pressure, $P_{w,sat}$, is only a function of temperature, T (Eq. (A.21)).

Table A.1
Overview of the experimental and numerical model parameters

Exp. nr.	Gas	T (°C)	P (bar)	$k_{rw,a}$ (–)	$k_{rg,a}$ (–)	λ_s (–)	σ (mN/m)	φ (–)	γ (–)	S_{wc} (–)	D_{50} (μm)	D_L (m)
4	N_2	24	1	0.5	1	3.84	71	0.37	0.51	0.1	400	0.01
6	CO_2	24	1	0.5	1	3.56	71	0.37	0.45	0.01	400	0.01
10	CO_2	28	8	0.5	1	7.32	67	0.38	0.49	0.075	400	0.01
11	N_2	27	8	0.5	1	6.18	71	0.37	0.46	0.075	400	0.01
12	CO_2	27	85	0.5	1	5.87	30	0.37	0.65	0.03	400	0.01

S_{wc}, λ_s and γ are adjustable model parameters, obtained by the least square curve fitting procedure (see Section A.3). The values for σ are obtained from Chun and Wilkinson [24] and are used to scale the P_c–S_w curves, shown in Figs. 10 and 11.

Table A.2
Summary of physical input parameters and variables used in the numerical model (roman characters)

Physical quantity	Symbol	Value	Unit
Sample area	A	$\frac{1}{4}\pi(0.084)^2$	m^2
Capillary number	Ca		–
Water vapor concentration	c_{gw}	Eq. (A.17)	mol/m^3
Gas concentration	c_{gg}	Eq. (A.13)	mol/m^3
Gas concentration in water	c_{wg}	Independent variable	mol/m^3
Diff. coeff. gas in water	D_g	From Gmelin [44]	m^2/s
Characteristic length	D_L	Model parameters	m
Average grain size	D_{50}	See Table A.1	m
Gravity constant	g	9.81	m/s^2
Sample height	h	25 (steel)/27 (PEEK)	mm
Henry's constant for CO_2	k_{Henry,CO_2}	From Duan and Sun [21]	Pa
Henry's constant for N_2	k_{Henry,N_2}	From www.henrys-law.org	Pa
Water, gas rel. perm.	k_{rw}, k_{rg}	Eq. (A.6)	m^3/m^3
Rock permeability	k	Eq. (A.5)	m^2
Atmospheric pressure	P_{atm}	1.0135×10^5	Pa
Gas pressure	P_g	Independent variable	Pa
Water pressure	P_w	P_w from $P_w = P_g - P_c$	Pa
Universal gas constant	R	8.3165	$\frac{m^3\ Pa}{mol^{-1}\ K^{-1}}$
Water saturation	S_w	Independent variable	m^3/m^3
Gas saturation	S_g	$S_g = 1 - S_w$	–
Residual gas saturation	S_{gr}	0 (used in the simulations)	m^3/m^3
Residual water saturation	S_{wc}	See Table A.1	m^3/m^3
Temperature	T	From experimental data	K
Gas injection rate	u_g^{inj}	From experimental data	m^3/s
Darcy gas/water velocity	u_g, u_w	Darcy's law, Eq. (A.4)	$\frac{m^3}{m^2\ s}$
Molar fraction gas in water	x_{gw}	Eq. (A.12)	–
Gas compressibility CO_2	z_g	From Span and Wagner [20]	–

Table A.3
Summary of physical input parameters and variables used in the numerical model (greek characters)

Physical quantity	Symbol	Value	Unit
Sorting factor	λ_s	Fitting parameter for Eq. (A.8) (see also Table A.1)	–
CO_2 viscosity	μ_{CO_2}	Fenghour et al. [22]	Pa s
N_2 viscosity	μ_{N_2}	1.8×10^{-5}	Pa s
Water viscosity	μ_w	Eq. (A.20)	Pa s
Water density	ρ_w	Eq. (A.19)	kg/m^3
CO_2 density	ρ_{CO_2}	Span and Wagner EOS [20]	kg/m^3
N_2 density	ρ_{N_2}	Ideal gas law, Eq. (A.14)	kg/m^3
Sample density	ρ_s	From experimental data	kg/m^3
Interfacial tension	$\sigma_{CO_2,w}$, $\sigma_{N_2,w}$	For CO_2: Chun and Wilkinson [24]; For N_2: 0.072	N/m
Rock porosity	φ	From helium measurements, see Table 1	m^3/m^3

The input parameters used for the numerical simulations are summarized in Table A.1. In each simulation the sand column is discretized into 10 layers. The characteristic length used for the mass transfer coefficient, k_L, is chosen as $D_L = 0.01$ m (Eq. (A.10)). The input capillary pressure curves are obtained from a least square curve fitting procedure, from which we estimate the coefficients, S_{wc}, γ and λ_s of the Leverett-J function, given by Eq. (A.8), using the experimental P_c–S_w curves (see Table A.1). The values for S_{wc}, λ_s and γ are adjustable model parameters and vary because different sand packing are used for each experiment. The capillary pressure, comparable to the measured capillary pressure, is derived from the pressure difference of the bulk phases and represented by

$$P_c = \left(P_{g,z=0} + \frac{\rho_g g H}{2}\right) - \left(P_{w,z=-L} - \frac{\rho_{wg} H}{2}\right). \tag{A.18}$$

The hydrostatic pressure correction for $P_{g,z=0}$ and $P_{w,z=-L}$ is due to placement of the PDT device in the experimental set-up (see Section 2.1 and Fig. 1).

A.4. Temperature and pressure dependent properties of N_2, CO_2 and water

The liquid water density, $\rho_w(T)$, viscosity, $\mu_w(T)$ and the water vapor pressure, $P_{w,sat}(T)$ are obtained from Tortike and Farouq Ali [47] (see also [46]), and are respectively given by

$$\begin{aligned}\rho_w(T) = {} & 3786.31 - 37.2487T + 0.196246T^2 \\ & - 5.04708\times10^{-4}T^3 + 6.29368\times10^{-7}T^4 \\ & - 3.08480\times10^{-10}T^5,\end{aligned} \tag{A.19}$$

$$\begin{aligned}\mu_w(T) = {} & -0.0123274 + \frac{27.1038}{T} - \frac{23527.5}{T^2} + \frac{1.01425e7}{T^3} \\ & - \frac{2.17342e9}{T^4} + \frac{1.86935e11}{T^5}\end{aligned} \tag{A.20}$$

and

$$\begin{aligned}P_{w,sat}(T) = {} & 103(-175.776 + 2.29272T - 0.0113953T^2 \\ & + 2.6278\times10^{-5}T^3 + 2.73726\times10^{-8}T^4 \\ & + 1.13816\times10^{-11}T^5)^2.\end{aligned} \tag{A.21}$$

A.5. Boundary conditions

Two sets of boundary conditions are considered for the drainage process:

(1) We consider a constant gas injection rate at $z = 0$ and a constant water pressure at $z = -L$.
(2) We consider a constant gas pressure at $z = 0$ and a constant water extraction rate at $z = -L$.

The volume change of the gas injection pump is incorporated using the expression:

$$\frac{1}{M}\frac{\partial \rho_{G,p} V_p}{\partial t} + A[c_{GG} u_g]_{z=0} = 0, \tag{A.22}$$

where $\rho_{G,p}$ is the density of the gas phase in the pump, V_p is the gas volume and A the sample area. Dependent on the boundary conditions, constant CO_2 injection or constant CO_2 pressure, we solve Eq. (A.22) for $P_{g,p}$ or V_p, respectively. Moreover, $u_w = 0$ at $z = 0$ and $u_g = 0$ at $z = -L$.

References

[1] Kumar A, Ozah R, Noh M, Pope GA, Bryant S, Sepehrnoori K, et al. Reservoir simulation of CO_2 storage in deep saline aquifers. SPE J 2005;10(3):336–48.
[2] Doughty C, Pruess K. Modeling supercritical carbon dioxide injection in heterogeneous porous media. Vadose Zone J 2004;3:837–47.
[3] Izgec O, Demiral B, Bertin H, Akin S. Experimental and numerical investigation of carbon sequestration in saline aquifers. Paper presented in SPE/EPA/DOE exploration and production environmental conference, Galveston, Texas, 2005.
[4] van Duijn CJ, de Neef MJ. The effect of capillary forces on immiscible two-phase flow in strongly heterogeneous porous media. Report, TU Delft. 1995.
[5] Morrow NR. Physics and thermodynamics of capillary action in porous media. Ind Eng Chem 1970;62(6):32–56.
[6] Hassanizadeh SM, Gray WG. Thermodynamic basis of capillary pressure in porous media. Water Resour Res 1993;29(10):3389–405.
[7] Reeves PC, Celia MA. A functional relationship between capillary pressure, saturation and interfacial area as revealed by a pore-scale network model. Water Resour Res 1996;32(8):2345–58.
[8] Anderson W. Wettability literature survey – part 4: effects of wettability on capillary pressure. JPT 1987;39(10):1283–300.
[9] van Lingen PP, Bruining J, van Kruijsdijk CPJW. Capillary entrapment caused by small-scale wettability heterogeneities. SPE Res Eng 1996;11(2):93–100.

[10] Jimenez JA, Chalaturnyk RJ. Integrity of bounding seals for geological storage of greenhouse gases. Paper presented in SPE/ISRM rock mechanics conference, Irving, Texas, 20–23 October, 2002.
[11] Chiquet P, Broseta D, Thibeau S. Capillary alteration of shaly caprocks by carbon dioxide. Paper presented in SPE Europec/EAGE annual conference, Madrid, Spain, 13–16 June, 2005.
[12] Plug W-J, Mazumder S, Bruining J, Siemons N, Wolf KH. Capillary pressure and wettability behavior of the coal–water–carbon dioxide system at high pressures. Paper presented at 2006 international CBM symposium, Tuscaloosa, Al., 22–26 May, 2006.
[13] Siemons N, Bruining J, Castelijns H, Wolf KH. Pressure dependence of the contact angle in a CO_2–H_2O–coal system. J Colloid Sci 2006;297(2):755–61.
[14] Siemons N, Bruining J, Wolf KH, Plug W-J. Pressure dependence of the CO_2 contact angle on bituminous coal and semi-anthracite in water. Paper presented at 2006 international CBM symposium, Tuscaloosa, Al., 22–26 May, 2006.
[15] Bennion B, Bachu S. The impact of interfacial tension and pore-size distribution/capillary pressure character on CO_2 relative permeability at reservoir conditions in CO_2–brine systems. Paper presented in SPE/DOE symposium on improved oil recovery, Tulsa, Oklahoma, USA, 22–26 April, 2006.
[16] Bennion DB, Bachu S. Supercritical CO_2 and H_2S–brine drainage and imbibition relative permeability relationships for intergranular sandstone and carbonate formations. Paper presented in SPE Europec/EAGE annual conference and exhibition, Vienna, Austria, 12–15 June, 2006.
[17] Spycher N, Pruess K, Ennis-King J. CO_2–H_2O mixtures in the geological sequestration of CO_2. I. Assessment and calculation of mutual solubilities from 12 to 100 °C and up to 600 bar. Geochim Cosmochim Acta 2003;67(16):3015–31.
[18] Ebigbo A, Bielinski A, Kopp A, Class H, Helmig R. Numerical modeling of CO_2 sequestration with mufte-ug. Paper presented in CMWR XVI, Copenhagen, June 2006.
[19] Class H, Helmig R, Bastian P. Numerical simulation of non-isothermal multiphase multicomponent processes in porous media – 1. An efficient solution technique. Adv Water Resour 2002;25:533–50.
[20] Span R, Wagner W. A new equation of state for carbon dioxide covering the fluid region from the triple-point temperature to 1100 K at pressures up to 800 MPa. J Phys Chem Ref Data 1996;25(6):1509–96.
[21] Duan Z, Sun R. An improved model calculation CO_2 solubility in pure water and aqueous NaCl solutions from 273 to 533 K and from 0 to 2000 bar. Chem Geol 2003;193:257–71.
[22] Fenghour A, Wakeham WA, Vesovic V. The viscosity of carbon dioxide. J Phys Chem Ref Data 1999;27(1):31–44.
[23] Wiebe R, Gaddy VL. The solubility of carbon dioxide in water at various temperatures from 12 to 40 °C and at pressures to 500 atmospheres. Critical phenomena. J Am Chem Soc 1940;62:815–7.
[24] Chun B-S, Wilkinson GT. Interfacial tension in high-pressure carbon dioxide mixtures. Ind Eng Chem Res 1995;34:4371–7.
[25] Pruess K, Garcia J. Multiphase flow dynamics during CO_2 injection into saline aquifers. Environ Geol 2002;42:282–95.
[26] Nordbotten JM, Celia MA, Bachu S. Injection and storage of CO_2 in deep saline aquifers: analytical solution for CO_2 plume evolution during injection. Transp Porous Media 2005;58(3):339–60.
[27] Christoffersen KR, Whitson CH. Gas/oil capillary pressure of chalk at elevated pressures. SPE Form Eval 1995;10(6):153–9.
[28] Jennings JW, McGregor DS, Morse RA. Simultaneous determination of capillary pressure and relative permeability by automatic history matching. SPE Form Eval 1988;3(3):322–8.
[29] Longeron D, Hammervold WL, Skjaeveland SM. Water–oil capillary pressure and wettability measurements using micropore membrane technique. Paper presented at international meeting on petroleum engineering, Beijing, 14–17 November, 1995. p. 543–53.
[30] Firoozabadi A, Aziz K. Relative permeability from centrifuge data. In: SPE California regional meeting, Oakland, California, 2–4 April, 1986.
[31] Newsham KE, Rushing JA, Lasswell PM, Cox JC, Blasingame TA. Comparative study of laboratory techniques for measuring capillary pressures in tight gas sands. Paper presented at SPE annual technical conference and exhibition, Houston, Texas, 26–29 September, 2004.
[32] Labastie A, Guy M, DelClaud JP, Iffly R. Effects of flow rate and wettability on water–oil relative permeabilities and capillary pressure. Paper presented in SPE annual technical conference and exhibition, Dallas, Texas, 21–24 September, 1980.
[33] Kalaydjian FJ-M. Dynamic capillary pressure curve for water/oil displacement in porous media: theory vs. experiment. Paper presented in SPE annual technical conference and exhibition, Washington, DC, 4–7 October, 1992. p. 491–506.
[34] Honarpour MM, Hunag DD, Dogru AH. Simultaneous measurements of relative permeability, capillary pressure, and electrical resistivity with microwave system for saturation monitoring. SPE J 1996;1(3):283–94.
[35] Topp GC, Klute A, Peters DB. Comparison of water content-pressure head data obtained by equilibrium, steady-state, and unsteady-state methods. Soil Sci Soc Am Proc 1967;31:312–4.
[36] Wanna-Etyem C. Static and dynamic water content-pressure head relations of porous media, Ph.D. thesis, Colorado State University, Fort Collins (CO), 1982.
[37] O'Caroll DM, Phelan TJ, Abriola LM. Exploring dynamic effects in capillary pressure in multistep outflow experiments. Water Resour Res 2005;41:1–14.
[38] Wildenschild D, Hopmans JW, Simunek J. Flow rate dependence of soil hydraulic characteristics. Soil Sci Soc Am J 2001;65:35–48.
[39] Hammervold WL, Knutsen O, Iversen JE, Skjaeveland SM. Capillary pressure scanning curves by micropore membrane technique. J Petrol Sci Eng 1998;20(3):253–8.
[40] Kokkedee JA. Simultaneous determination of capillary pressure and relative permeability of a displaced phase. Paper presented at European petroleum conference, London, 25–27 October, 1994. p. 213–22.
[41] Plug W-J, Slob E, Bruining J, Moreno-Tirado LM. Simultaneous measurement of hysteresis in capillary pressure and electric permittivity for multiphase flow through porous media. Geophys Lett 2007;72(3):A41–5.
[42] Mazumder S, Plug W-J, Bruining J. Capillary pressure and wettability behavior of coal–water–carbon dioxide system. Paper presented at SPE annual technical conference and exhibition, Denver, Co. 5–8 October, 2003.
[43] van Lingen PP. Quantification and reduction of capillary entrapment in cross-laminated oil reservoirs, Ph.D. thesis, Delft University of Technology, 1998.
[44] Gmelin L. Gmelin Handbuch der Anorganischen Chemie, 8, Auflage Kohlenstoff, Teil C3, Verbindungen, 1973.
[45] Bird RB, Steward WE, Lightfoot EN. Transport phenomena. New York: John Wiley and Sons; 1960.
[46] Bruining J, Marchesin D. Analysis of nitrogen and steam injection in a porous medium with water. Transp Porous Media 2006;62:251–81.
[47] Tortike W, Farouq Ali SM. Saturated-steam-property functional correlations for fully implicit reservoir simulation. SPE Res Eng 1989;4(4):471–4.